Tropical Intraseasonal Oscillation Appearing in Operational Analyses and in a Family of General Circulation Models

SILVIO GUALDI AND ANTONIO NAVARRA

IMGA-CNR, Modena, Italy

HANS VON STORCH

Institute of Hydrophysics GKSS Research Center, Geesthacht, Germany

(Manuscript received 2 June 1995, in final form 14 October 1996)

ABSTRACT

The statistics of tropical intraseasonal variability are studied using European Centre for Medium-Range Weather Forecasts analyses and several ECHAM General Circulation Model experiments made with different model versions (ECHAM2 and ECHAM3, which have different convection schemes) and different horizontal resolutions (T21, T42, and T106). The study applies the principal oscillation pattern technique to the 200-mb equatorial velocity potential. Associated patterns of tropical outgoing longwave radiation, equatorial zonal wind, and equatorial divergence are also presented.

The intercomparison of ECHAM2 and ECHAM3 simulations at low (T21) resolution shows that the improved model physics has a beneficial impact on the simulated Madden–Julian oscillation (MJO). The MJO produced by the ECHAM2 model has an unrealistic spatial distribution of convection, whereas the MJO simulated by the ECHAM3 model appears to be related to convective activity over the Indian Ocean and the West Pacific, which is consistent with the observed MJO.

An increase of the horizontal resolution of the ECHAM3 model seems to actually degrade the results. At T42 and T106, the ECHAM3 MJO exhibits too much convective activity over central and equatorial America, with only a marginal effect of the MJO on the West Pacific–Indonesian region.

1. Introduction

The tropical intraseasonal oscillation, first detected by Madden and Julian in 1971 (Madden and Julian 1971; for a comprehensive review see Madden and Julian 1994) is the strongest regular tropical signal on the subseasonal timescale. The oscillation, also known as the Madden–Julian oscillation (MJO), is a large-scale eastward propagating disturbance, originating between the Indian Ocean and Indonesian region. The MJO period spans a wide range in the intraseasonal timescale. It represents one of the most important physical phenomena of the tropical troposphere; it interacts with the monsoon (Lorenc 1984), induces low-frequency variability in the extratropics (Ferranti et al. 1990), and may be one of the quasi-random processes of the equatorial troposphere triggering the development of El Niño–Southern Oscillation events (Lau and Chan 1986, 1988). It is reasonable to conclude that the understanding of the dynamics of the MJO is an important issue, and the quality of its simulation by general circulation models (GCMs) an important component of the assessment of the model.

Previous empirical analyses (Madden and Julian 1971; Weickmann et al. 1985; Lau and Chan 1985; Knutson and Weickmann 1987; von Storch and Xu 1990; Hendon and Salby 1994; Slingo et al. 1995) have revealed the following properties of the MJO:

1) The oscillation is mainly active in the Tropics. In several variables (e.g., velocity potential, zonal wind) it exhibits a predominant zonal wavenumber one spatial pattern. If no seasonal stratification is performed, the MJO appears mostly symmetric to the equator; however, in different seasons major asymmetries develop.
2) The oscillation is not strictly periodic, but has a preferred timescale ranging between 20 and 80 days, with the most frequent occurrence near 45 days.
3) Tropical convection and tropical circulation anomalies associated with the oscillation tend to propagate eastward with time.
4) The mode exhibits two distinctly different phases:
   (a) A "wet–slow" phase that can be identified when the maximum upper-level divergence is in the convectively active areas (Indian Ocean, West

Corresponding author address: Dr. Silvio Gualdi, IMGA-CNR, via Emilia Est 770, 41100 Modena, Italy.
E-mail: gualdi@nabucco.bo.cnr.it

Pacific, and South America). In this phase, the propagation speed is relatively slow (of the order of $\simeq 5$ m s^{-1}), and the amplitude of the mode intensifies. There is a well-defined signature in the low-level flow, in the outgoing longwave radiation (OLR) and in the precipitation.

(b) A "dry–fast" phase appears to set in when the disturbance moves through areas of small convective activity (central–eastern Pacific, Atlantic), with a faster velocity of propagation (about 30 m s^{-1} in surface pressure and about 15–20 m s^{-1} in upper velocity potential and zonal wind) and no signature in OLR, precipitation, and low-level circulation. In this phase, the amplitude of the mode tends to decrease.

5) In the wet–slow phase a characteristic zonal displacement in the vertical distribution of convergence takes place, as the convergence anomalies aloft shift several tens of degrees west with respect to those at the surface.

The dynamical mechanisms responsible for the MJO are not fully understood. Since the oscillations originate predominantly over the Indian Ocean, propagate eastward with equatorial maximum and trapping, and apparently do not show any significant meridional wind perturbation (Madden and Julian 1972), they are interpreted as a Kelvin wave induced by strong outbreaks of convective activity. Lau and Peng (1987) and Chang and Lim (1988) suggested that the conditional instability of the second kind (CISK) mechanism could enable the Kelvin waves to propagate around the globe. In the CISK mechanism, low-level convergence provides enough humidity to sustain moist convection. Wang (1988) showed that some of the main dynamical characteristics of the tropical low-frequency waves can be explained by a theoretical model in which the boundary layer frictionally induced moisture convergence (frictional wave CISK) is taken into account. In a recent observational study Hendon and Salby (1994) computed a composite life cycle of the MJO signal present in 11 years (1979–89) of European Centre for Medium-Range Weather Forecasts (ECMWF) and National Meteorological Center (NMC), now the National Centers for Environmental Prediction, analyses. In agreement with the results previously found in the First GARP (Global Atmospheric Research Program) Global Experiment dataset and in the Geophysical Fluid Dynamics Laboratory (GFDL) climate model by Hayashi and Golder (1988), they found that surface convergence is shifted some 40°–50° longitude east of inviscid convergence at 850 mb and that the convergence is produced predominantly by meridional flow into the near-equatorial surface low. The composite structure of the MJO supports frictional wave CISK as an important mechanism underlying the MJO.

The wave-CISK model, however, is not the only existing theory for the MJO. Alternative mechanisms like the "thermal forcing" theory or the "evaporation–wind feedback instability" theory have been suggested by Yamagata and Hayashi (1984), Neelin et al. (1987), and Emanuel (1987), respectively. A brief theoretical review of the MJO can be found in Hayashi and Golder (1993).

TABLE 1. Summary of the analyzed datasets.

Experiment	Resolution	Length of run
	ECHAM runs	
ECHAM2	T21	20 years
ECHAM3T21	T21	30 years
ECHAM3T42	T42	30 years
ECHAM3T106	T106	3 years
	ECMWF analyses (1990–92)	
ECMWF	T106	3 years

In the last few years an increasing interest in the ability of GCMs to simulate the tropical intraseasonal oscillation has developed. Several MJO GCM intercomparison studies (e.g., Park et al. 1990; Slingo et al. 1995) have yielded considerable insight into how models represent the MJO and into our general understanding of the MJO. The scope of the present paper is to investigate the MJO performance in a series of climatological simulations, performed with different versions of the ECHAM atmospheric GCM, using an approach already established by von Storch and Xu (1990). A further aim of the paper is to verify the results of von Storch and Xu (1990) with an independent dataset, namely the 6-h operational T106 analyses prepared by the ECMWF from January 1990 to December 1992. This dataset is also used to verify the MJO in the new ECHAM climatological simulations.

A climatological simulation is an extended experiment performed with climatologically prescribed sea surface temperature and sea ice distributions. The model versions that are compared are the second (ECHAM2) and the third (ECHAM3) generations of the ECHAM model. A list of the experiments is given in Table 1.

Other numerical experiments have been studied by Slingo et al. (1995), where the MJO simulated by 15 GCMs has been analyzed, and Hayashi and Golder (1993), who examined the oscillation appearing in the 1979–87 ECMWF dataset and in a GFDL climate model with moist convective adjustment.

The main statistical approach taken in this study is to calculate the principal oscillation patterns (Hasselmann 1988; von Storch et al. 1988; for a general review see von Storch et al. 1995). This approach was already successfully used by von Storch and Xu (1990) to examine the MJO in operational NMC analyses from 1985 to 1989. The principal oscillation pattern (POP) analysis is here performed on the 200-mb equatorial velocity potential (equatorial χ_{200}), for timescales between 15 and 90 days. The equatorial upper air χ was chosen to study the oscillation rather than, for example, the wind com-

ponents or the OLR, because the oscillation has a strong signature in this field. The velocity potential is not a locally measurable quantity; it is the inverse Laplacian of divergence and can be regarded as a grossly smoothed divergence field that overemphasizes the larger scales. The χ field provides a "first-order" description of the gross repeatable features of the oscillation, and therefore is a good choice for the comparison of the basic characteristics of the oscillation obtained from different simulations.

After the dominant POPs have been identified for the key variable (equatorial χ_{200}), additional insight into the structure of the tropical oscillation has been obtained by calculating composite and correlation analyses to yield the patterns of OLR, zonal wind, and divergence that are associated with the MJO.

In section 2, a description of the observed data and the different versions of the ECHAM model are presented. In sections 3 and 4, the results of the POP analyses are presented and discussed for the ECMWF analyses and for the ECHAM models. In section 5, a summary and some discussion complete the paper.

2. Description of the datasets used in this study

The modeling results employed in this work are time series obtained from climatological experiments performed with the ECHAM2 and the ECHAM3 GCMs. The ECHAM model has been developed at the Max-Planck-Institut für Meteorologie in Hamburg, and it is an evolution of the numerical weather prediction model developed at ECMWF. An exhaustive and detailed description of the ECHAM GCMs and their capability to reproduce the main features of the observed general circulation has been given by Roeckner et al. (1992).

In the successive model generations, several parameterization schemes were either replaced or additionally implemented. The second- and the third-generation models differ mainly in their convection schemes, namely, ECHAM2 uses the Kuo scheme (Kuo 1974), whereas ECHAM3 is implemented with the Tiedtke convection scheme (Tiedtke 1989).

In the Kuo parameterization scheme, the penetrative convection is based on a moisture convergence closure hypothesis: convection occurs wherever there is a deep layer of conditional instability and large-scale moisture convergence. In this scheme the amount and the vertical distribution of latent heat released by the convection is calculated from the moisture convergence and temperature difference between the cloud and the environment (Kuo 1974).

The Tiedtke scheme is based on the same general assumptions, but expressed in terms of moisture and mass convective fluxes. The link between cloud mass flux and large-scale moisture convergence provides profiles of convective mass fluxes and heating in good agreement with observations. In particular, it has been shown (Tiedtke 1989) that the diabatic forcing of the tropical large-scale flow, and the vertical circulation in response to heat sources over the West Pacific and the Indian Ocean, appear more realistic than those obtained with the Kuo parameterization. Therefore, since it is generally believed that the intraseasonal variability is strongly affected by equatorial convection, some differences in the ECHAM2 and ECHAM3 MJO are to be expected.

In order to assess the impact of increased horizontal resolution on the simulated oscillation, three horizontal resolutions of the ECHAM3 model (triangular truncation 21, 42, and 106, hereafter T21, T42, and T106, respectively) have been used in the analysis. The surface boundary conditions correspond to the climatological annual cycle, with no interannual anomaly forcing.

The MJO simulated in the different experiments has been compared with the MJO in ECMWF analyses, using time series calculated from four-times daily analyses from January 1990 to December 1992. A global and detailed description of the analyses has been given by Trenberth (1992). In May 1989 the ECMWF analysis scheme was substantially modified, with major changes in the convective parameterization, radiation, and gravity wave drag (Trenberth 1992). These changes can lead to significant changes in the ECMWF analysis data, especially over areas with low observational data density (Arpe 1990). Therefore, in order to have homogeneous data, we have decided to restrict our analysis to the period 1990–92. Table 1 gives a list of the experiments and analysis datasets that have been used in this study.

In addition to the ECMWF analyses, a dataset of observed OLR from the National Oceanic and Atmospheric Administration (NOAA) has been employed to compute OLR composite patterns. These data have already been used in several studies (e.g., Salby and Hendon 1994; Ju and Slingo 1995), and their relation to tropical precipitation has been demonstrated by Arkin and Ardanuy (1989).

An example of the capability of the model to reproduce the climatological χ_{200} and OLR fields is given in Fig. 1. Here the January and the July mean fields simulated by the ECHAM3T106 model are shown, together with the fields obtained from the ECMWF analyses and observed OLR.

In the Eastern Hemisphere, the strong gradient of velocity potential is well reproduced over the Indonesian region in January (Fig. 1a) and over the Indian Ocean in July (Fig. 1b). The minimum in observed OLR is shifted about 30° westward from the minimum of χ_{200}, whereas in the GCM simulation, the minimum of OLR and velocity potential overlap at about 150°E.

In the Western Hemisphere, the model fails to simulate the gradient of velocity potential over South America in January (Fig. 1a), and, from both the OLR and the χ fields, it is also evident that the model tends to produce an excess of convective activity over Central America in the northern summer (Fig. 1b).

The main features of the 200-mb χ and OLR fields

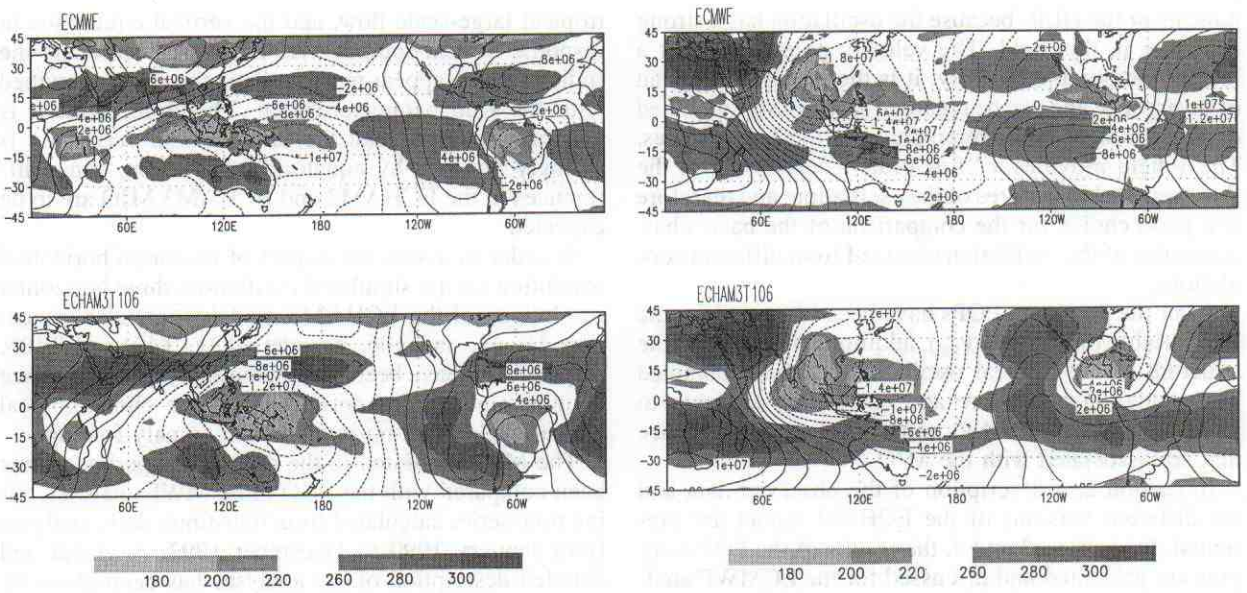

FIG. 1. (a: left) January mean 200-mb velocity potential and OLR: (upper panel), ECMWF analyses and NOAA OLR observations, (lower panel) ECHAM3T106. Contour: χ (contour lines) $2 \cdot 10^6$ m^2 s^{-1}, OLR (shaded areas) 20 W m^{-2}. (b: right) Same as (a) but for July mean.

simulated by the T106 version of the ECHAM3 model are basically common to all of the ECHAM models considered here. However, it was found that the tendency to simulate an overproduction of convection over Central America, common to the higher-resolution versions of ECHAM3 (T42 and T106), is less pronounced at the lower-resolution T21 (not shown).

The POP analysis was carried out for the 200-mb velocity potential field along the equator, averaged meridionally between 5°N and 5°S. Since we are interested in a timescale of a few weeks, all of the original time series, before the POP analysis, were filtered to suppress signals with periods longer than 90 days and shorter than 15 days. A Fourier filter was used, where the filter window has cosine "tails" to suppress the secondary maxima that might occur for a pure "rectangular" filter (von Storch et al. 1995). Moreover, in order to suppress small-scale noise and to reduce the dimensions of the system, an EOF expansion of the χ_{200} time series was performed. The expansion was truncated after 10 terms and the truncated series retain more than 95% of the filtered variance.

After the POPs are defined for χ_{200}, the time coefficients of the patterns, that is, the POP coefficients, are taken as a bivariate index of the oscillation. Associated patterns are derived for additional tropical field variables using correlation and composite techniques applied to tropical (30°N–30°S) OLR and 200-mb velocity potential, equatorial 200-mb zonal wind, and equatorial divergence at six different pressure levels.

Before applying the POP analysis, a basic "eyeball" analysis of the tropical intraseasonal oscillation was performed by means of time–longitude (Hovmöller) diagrams of the equatorial (average between 5°N and 5°S), band-pass filtered, χ_{200} anomaly time series, for both the ECMWF analyses and the ECHAM experiments. The Hovmöller diagrams (not shown) always indicated the existence of a wavenumber one eastward propagating disturbance.

In the ECMWF analyses, the waves can be seen more clearly during the northern winter and spring. Their largest amplitudes occur in the Eastern Hemisphere, with two maxima of activity over the Indian Ocean and between the Indonesian region and the date line. From this visual inspection, there was some evidence of a generally faster velocity of propagation over the Western Hemisphere, consistent with the results of von Storch and Xu (1990), Weickmann and Khalsa (1990), and Slingo et al. (1995). In the Eastern Hemisphere, across the Indian Ocean, the Maritime Continent and the West Pacific, the propagation of the disturbance seemed to be characterized by alternating growth and decay, accompanied by slowdown and acceleration. In contrast to observed variability, the occurrence of the GCM simulated traveling disturbances did not seem to be related to a specific season of the year.

The POP analysis of χ_{200} produces, in all cases, one POP pair that is by far dominant over the others. The characteristics of these POPs are shown in Table 2.

In all cases, the dominant POP pair explains more than 50% of the total filtered variance, and their periods are in the range 36 (ECHAM3T106) to 42 days (ECMWF). The period of the tropical intraseasonal oscillation simulated by GCMs has been shown to be sensitive to physical parameterization, especially to the Kuo convective scheme (Kuma 1990, 1994), that is em-

TABLE 2. Characteristics of the dominant POP of band-pass filtered equatorial velocity potential.

Experiment	Period (day)	Expl. Variance
ECHAM runs		
ECHAM2	39	61%
ECHAM3T21	37	61%
ECHAM3T42	40	58%
ECHAM3T106	36	50%
ECMWF analyses (1990–92)		
ECMWF	42	63%

ployed in ECHAM2. ECHAM3 uses the Tiedtke convective parameterization scheme and it is possible that this alters the MJO in ECHAM3, but a detailed investigation of this issue is outside the scope of this paper.

To assess the robustness of the estimated POP periods, a cross-spectral analysis of the POP coefficient (real and imaginary parts) time series has been performed for each dominant POP. In all cases the cross-spectral analysis (not shown) revealed well-defined maxima of variance centered on the estimated periods (Table 2) and covering a relatively broad period range (e.g., 25–60 days for the ECMWF analyses; 20–50 days for ECHAM2; 30–50 days for ECHAM3T106). Throughout this range there is also a fairly constant phase difference of about −90° between the real and the imaginary parts of the coefficients, and peaks of coherence squared (more than 75%) are found in the period range estimated by the POP.

All these features indicate that the POPs found are consistent with the POP model (von Storch et al. 1995) and that they are representative of genuine intraseasonal oscillations in a relatively broad period range that is consistent with the POP period.

For the sake of simplicity we will split the presentation of the results into two parts, showing first the "reference" results obtained from the ECMWF analyses and then the results for the various GCM runs.

3. Results: The MJO in the ECMWF analyses

The orthogonal POP patterns p_{re} and p_{im}, normalized according to von Storch et al. (1988), are shown in Fig. 2. They exhibit a wavenumber one spatial structure, with a phase shift between the real and the imaginary parts of about 90°; hence, according to the POP concept, they appear in sequence of the type

$$\cdots \rightarrow p_{re} \rightarrow -p_{im} \rightarrow -p_{re} \rightarrow p_{im} \rightarrow p_{re} \rightarrow \cdots,$$

describing an eastward traveling signal. The maximum of anomaly velocity potential, which is initially located over the Indian Ocean, propagates during one-quarter of a period (about 10 days) from about 70°E in $-p_{re}$, to near 130°E, where we find the largest extreme in p_{im}. After another quarter of a period a p_{re} has evolved, moving the maximum across the date line at about 160°W.

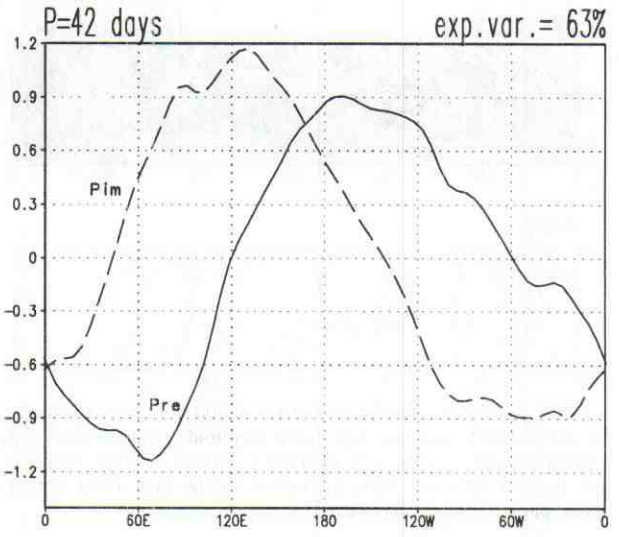

FIG. 2. Spatial structure of the first POP pair, ECMWF analyses. Normalization according to von Storch et al. (1988), with orthogonal patterns p_{re} and p_{im}.

Here the amplitude of the disturbance has substantially decreased. Finally, about 30 days after the starting of the cycle, the maximum has moved to about 60°W in $-p_{im}$. In accordance with observations and with previous studies, most of the activity is confined to the Eastern Hemisphere between 60° and 130°E where we find the largest extremes and, consequently, the steepest gradients. This result also confirms the longitudinal variation of the phase speed already noticed in previous studies (e.g., von Storch and Xu 1990; Slingo et al. 1995). In fact, the maximum of the oscillating mode takes half a period (about 20 days) to propagate from the Indian Ocean to the date line (about 120° longitude), and the remaining half a period to move from slightly east of the date line to the Indian Ocean (about 240° longitude).

a. Associated correlation patterns

The associated correlation patterns are the patterns q that yield the best specification of the field $y(t)$ using the POP coefficients $a(t)$. In other words, if a pair of POPs, p_{re} and p_{im}, is identified in the "key" variable (in this case the 200-mb equatorial velocity potential), and $a^1(t)$ and $a^2(t)$ are the time coefficients of the POPs, then the signal's appearance in another variable, $y(t)$, may be identified by means of the associated correlation patterns q_{re} and q_{im}, defined by

$$\left\langle \left\| y(t) - \frac{a^1(t)}{\sigma_1} q_{re} - \frac{a^2(t)}{\sigma_2} q_{im} \right\|^2 \right\rangle = \min,$$

where σ_i^2 is the variance of a^i.

These patterns are interpreted in a similar way to the POPs themselves; if the POPs perform one cycle, $\cdots \rightarrow p_{re} \rightarrow -p_{im} \rightarrow -p_{re} \rightarrow p_{im} \rightarrow p_{re} \rightarrow \cdots$, the associated

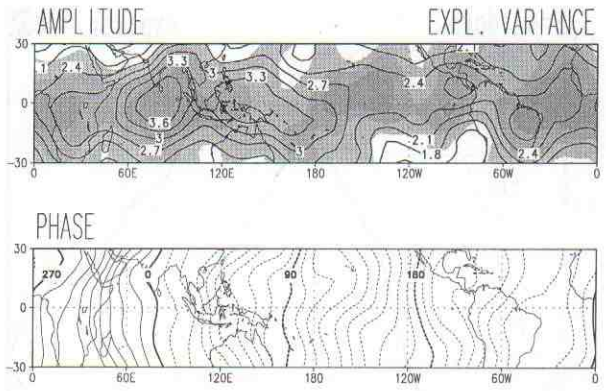

FIG. 3. Associated correlation patterns of 200-mb velocity potential for the ECMWF analyses. Top panel: amplitude (contour line, with contour interval $3 \cdot 10^5$ m^2 s^{-1}), explained variance (shaded, with contour interval 10% and white for values smaller than 40%); bottom panel: phase (contour interval 10°).

correlation patterns do the same: $\cdots \rightarrow q_{re} \rightarrow -q_{im} \rightarrow -q_{re} \rightarrow q_{im} \rightarrow q_{re} \rightarrow \cdots$.

In order to show not only the patterns but also the characteristic magnitude, the associated patterns have been multiplied by the standard deviation of the POP coefficients.

The mode patterns may also be represented in terms of local wave amplitude $A^2(\mathbf{r}) = [p_{re}^2 + p_{im}^2]^{1/2}$ and relative phase $\psi(\mathbf{r}) = \tan^{-1}[p_{re}/p_{im}]$. The choice of the "zero phase" is arbitrary, and we defined it as the angle at which the maximum amplitude occurs.

The amplitude–phase representation turns out to be particularly useful in our study as it permits the comparison between various cases and avoids the problem of arbitrariness in selecting real and imaginary components for a POP.

Associated correlation patterns of the χ_{200} over the tropical belt (Fig. 3) have been computed to check whether relevant information was disregarded when confining the POP analysis to the equator. The amplitude (solid isolines) and the explained variance (shaded areas) are shown in the upper panel and the phase in the lower panel. As expected, the patterns along the equator reproduce the equatorial POP patterns and exhibit essentially the same propagation features. The oscillation is well defined over the entire tropical belt, with largest amplitude near the equator. The maximum values of amplitude are of the order 3.6×10^6 m^2 s^{-1} and they occur in the equatorial eastern Indian Ocean–Indonesian region, coincident with the largest values of explained variance. Furthermore, a tongue of large amplitude values extends along the equator across the Indonesian region to the date line. Since our patterns are not stratified by season, it is likely that the shape of the maximum amplitude is an average of the maximum amplitude detected by Madden (1986) in the Indian Ocean and Indonesian region in the northern summer and northern winter seasons, respectively.

The smallest values of amplitude occur in the central–eastern Pacific, between 150°W and South America, where they are about 2.4×10^6 m^2 s^{-1}. The patterns tend to be symmetric with respect to the equator, though the symmetry is interrupted in areas like the southern tip of India, where the activity extends northward into the Bay of Bengal, probably related to the Indian monsoon. Also, between the Indonesian region and the date line, there is a tendency for the maximum amplitude to migrate southward over the Southern Pacific convergence zone (SPCZ), whereas in the eastern Pacific, off the Central American coast, the local maximum is shifted northward, overlapping the position of the intertropical convergence zone (ITCZ).

The POP mode represented by the patterns in Fig. 3 behaves like an inhomogeneous wave, namely a wave with spatially varying phase (Born and Wolf 1975), and the curves of constant phase are the two-dimensional equivalent of the wave surface. A local phase velocity can then be defined by the local derivative of the phase pattern, as

$$v_\phi = \frac{\omega}{\nabla\phi \cdot \mathbf{q}},$$

where ω is the frequency of the mode, $\mathbf{q}$ the unit vector in the direction of propagation, and ϕ the phase.

Accordingly with the equatorial POP patterns, the larger number of phase curves indicates that the disturbance spends a longer time in the Eastern Hemisphere than in the Western Hemisphere. Therefore, the propagation of the tropical mode also seems to be, on average, slower in the Eastern than in the Western Hemisphere, even if important exceptions can be found, like the substantial slowdown over the ITCZ.

There is also some evidence of a correlation between the phase velocity and the amplitude of the mode: immediately after a decrease of amplitude there is an acceleration, and, conversely, an increase of amplitude is always followed by a slowdown. This velocity–amplitude relationship is evident over equatorial Africa and the Indonesian region and can also be seen over the SPCZ region.

The characteristics of the disturbance highlighted by the mode represented in Fig. 3 are in agreement with the "four-stage life cycle" of the oscillation suggested by von Storch and Xu (1990) and by Rui and Wang (1990): "Initiation over equatorial Africa; rapid development while passing through the equatorial Indian Ocean; mature evolution characterized by an intermittent weakening over Indonesia and re-intensification over the western Pacific warm pool; and a final decay near the date line or emanation from the equatorial central Pacific toward subtropical North America and the southeastern Pacific." As it has been shown by von Storch and Xu (1990), the four-stage life cycle is then modulated by the seasonal cycle, which causes a southward (northward) displacement of the track of the oscillation during the northern winter (northern summer).

b. Associated composite patterns

More explicit and detailed information about the time behavior of the traveling disturbance are given by composite patterns. The construction of composite patterns with respect to the values of a base index (or indices) is a general technique widely used in atmospheric and oceanic research. In this study the base indices are derived from the bivariate time series of the complex coefficients $a(t)$ of the dominant POP pair. Following von Storch et al. (1988), we take as indices the modulus $L(t)$ and the phase $\delta(t)$ of the complex number $a(t)$. We divide the complex plane into a set of eight regions (index classes): $K1$, $K2$, ···, $K8$. Then the composite patterns (for the set of classes) are obtained by averaging over all vectors, $y(t)$, for which the associated indices fall into a given class. In order to consider only significant contributions, each class is bounded on the inside by a lower bound limitation on the magnitude of $L(t)$: $L > \langle L \rangle + d\sigma_L$, where σ_L is the standard deviation of L and we have (arbitrarily) set the coefficient $d = 0.8$.

In this way we construct a kind of pseudo Hovmöller diagram, where the evolution of the anomaly extremes and their behavior as a function of the phase velocity are explicitly shown.

1) 200-MB TROPICAL χ AND OLR

The associated composite patterns of the 200-mb anomalous velocity potential together with observed anomalous OLR in the Tropics are shown in Fig. 4. As we have divided the complex plane into eight classes, the entire period will be divided by eight, and therefore the passage from one class to another corresponds to a time step of about 5 days.

Since in our convention OLR is negative, positive anomalies of OLR are associated with enhanced convection and negative OLR anomalies with reduced convection. Therefore, the composites show us the relative evolution of the anomalous convection and divergent flow signals associated by the POP analysis to the MJO.

The associated OLR patterns explain more than 10% of the filtered variance over most of the Tropics, with maxima larger than 25% over equatorial Africa, the Maritime Continent, the SPCZ and ITCZ regions, the equatorial eastern Pacific, and equatorial America.

The velocity potential composite patterns exhibit a zonal wavenumber one structure covering the entire Tropics. Like the associated correlation patterns, the composites reproduce along the equator the equatorial POP patterns, and their amplitudes decrease symmetrically away from the equator. Since the composites are constructed from episodes for which the coefficient amplitude $L(t)$ exceeds the mean by at least 0.8 standard deviations, the magnitudes of the composite patterns are systematically larger than the magnitudes of the associated correlation patterns, which are calculated from all states.

In the first composite, a negative anomaly of velocity potential and a positive anomaly of OLR (associated with convection) are centered over the Indian Ocean at about 60°E, while a relative χ maximum and OLR minimum, linked to the previous cycle of the oscillation, are lying across the date line, shifted about 10° south, over the SPCZ.

In the growing phase of the disturbance (Indian Ocean), the anomalies of χ and convection are in phase, whereas the anomalies linked to the decaying phase of the oscillation (date line) have their maxima shifted some 30° longitude.

After about 5 days the χ negative anomalies have moved eastward to about 90°E in phase with the anomalous convection. The χ negative anomalies attain the largest amplitude of the whole cycle, at about -6×10^6 m^2 s^{-1}. The anomaly extremes are also shifted slightly northward relative to the equator, penetrating the Indian monsoon activity area. The positive χ anomaly has moved quickly through the eastern Pacific to Central America, where its amplitude has increased. Here it is approximately in phase with the negative anomaly of OLR developing off the Central American coast.

The sequence of the composite patterns allows us to roughly estimate the velocity of propagation of the disturbance. Between composite 1 and composite 2, the minimum of velocity potential and the convective anomaly move from about 60°E to about 90°E in 5.25 days, therefore they have moved with a velocity of propagation of about 8 m s^{-1}.

In composite 3 the minimum of χ and the maximum of enhanced convection are still in phase and approximately located at 130°–140°E. Therefore, the disturbance has slightly accelerated through the eastern part of the Indian Ocean, propagating with a velocity of about 12 m s^{-1}. Later (composites 4 and 5) the disturbance slows down again over the western Pacific warm pool, moving very slowly, roughly 5–6 m s^{-1}, between the Indonesian region and the date line.

Between composite 3 and composite 5, the convection anomaly seems to move slightly slower than the minimum of χ, and, in composite 5, after the negative anomaly of velocity potential has crossed the date line, the two fields are no longer in phase. The anomalies that cross the date line tend to migrate south by about 10–15° to cover the SPCZ region. Also in the eastern Pacific, anomalies develop slightly north of the equator indicating the influence of the ITCZ activity on the oscillation. In the meantime positive anomalies of χ and suppressed convection are evolving in phase over the convective areas of South America, and a new cell of positive χ anomaly is developing over Africa and the Indian Ocean (composite 3–5).

In the subsequent composites (6 and 7), the negative anomalies of χ travel quickly, about 20 m s^{-1}, through the eastern Pacific and then slow down over South America, where there is also an increase in the amplitude. Even if there is some convective activity, growing

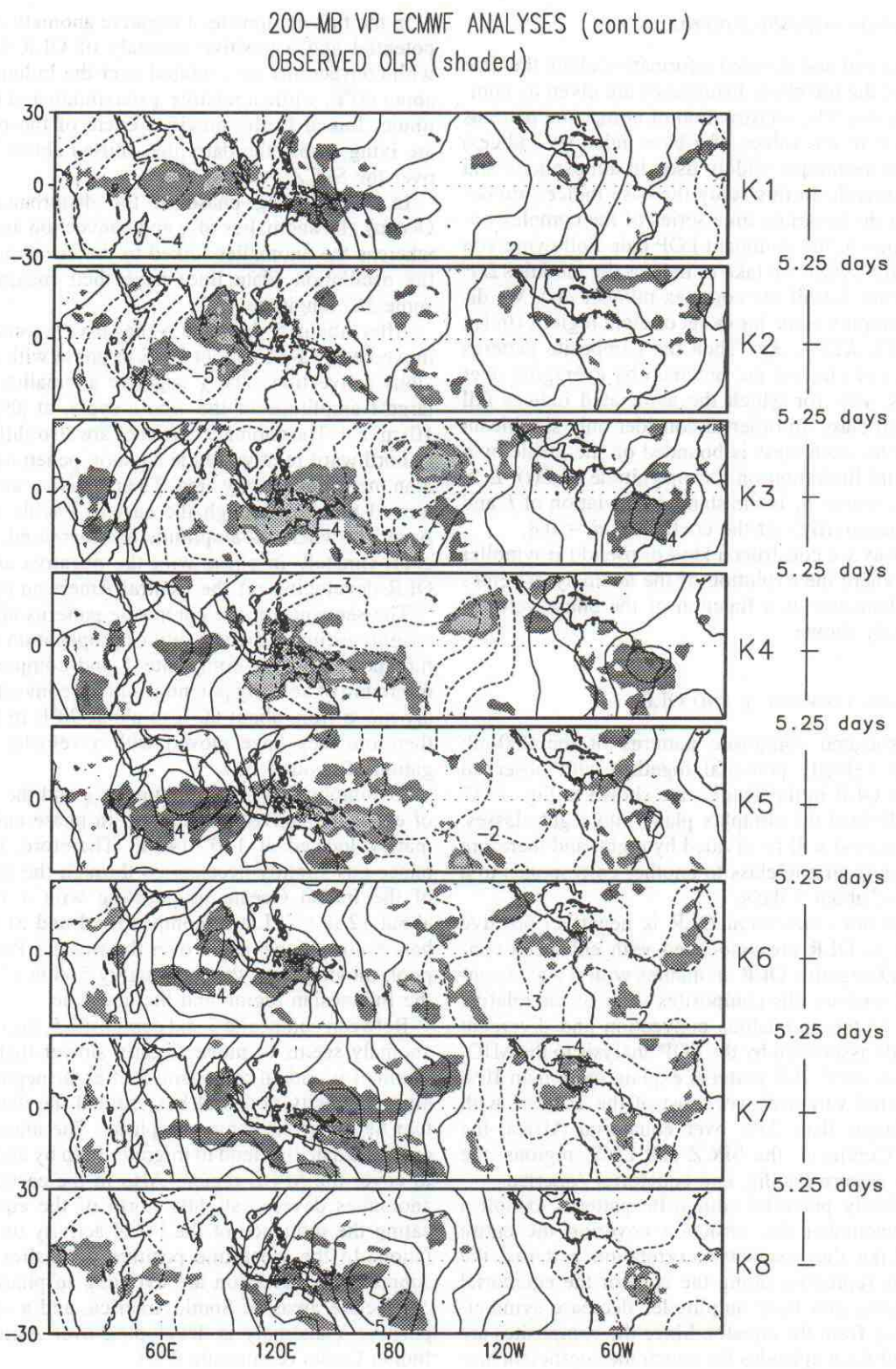

FIG. 4. Composites K_i of tropical 200-mb velocity potential anomaly from ECMWF analyses (contour line) and observed OLR anomaly (shaded). The ith panel shows composite K_i. Contour line interval is $1 \cdot 10^6$ m^2 s^{-1}; shaded contour interval is 10 W m^{-2}. Light shaded areas indicate positive anomalies of OLR (enhanced convection); dark-shaded areas indicate negative anomalies of OLR (reduced convection).

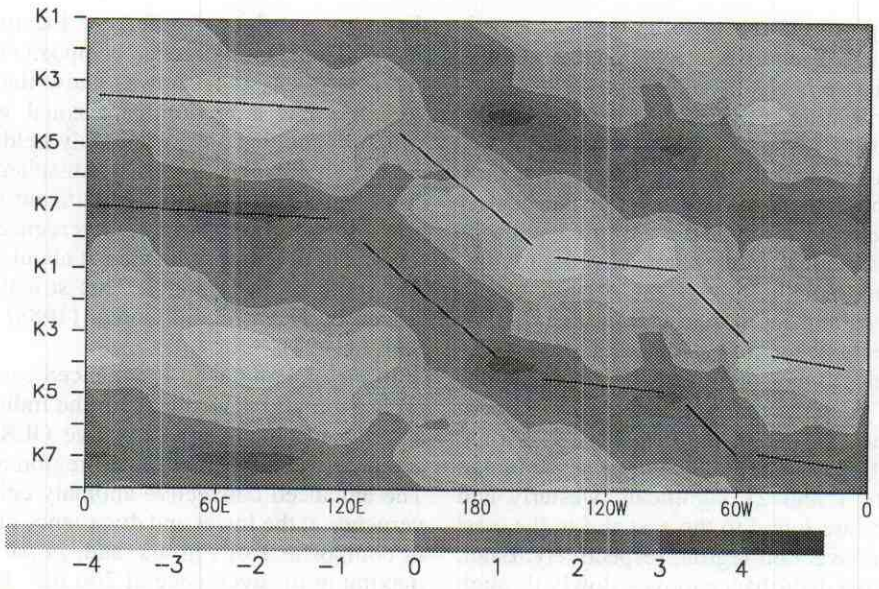

FIG. 5. Hovmöller representation of the composites K_i of equatorial 200-mb zonal wind anomaly from ECMWF analyses. Two cycles are shown. Contour interval is 1 m s^{-1}.

in phase with χ over Central America and northeast Brazil, it is less significant than that in the Eastern Hemisphere. The cell of positive anomaly, in turn, moves from the Indian Ocean to the west Pacific, closely in phase with the convective signal.

The cycle is closed by the sequence of composites 7, 8, and 1, respectively, where the minimum of velocity potential moves from equatorial South America to equatorial Africa in about 5 days, with a phase velocity of approximately 25 m s^{-1}. Afterwards, between composite 8 and composite 1, the χ and the convective anomalies move again in phase from equatorial Africa to the Indian Ocean.

In the growing phase of the disturbance (first four composites for the negative anomalies and last four for the positive anomalies), the anomalies of 200-mb velocity potential and convection grow in phase, moving slowly (from about 5–6 m s^{-1} to about 12 m s^{-1}) eastward from the Indian Ocean to the date line (wet–slow phase of the oscillation). In the decaying phase, on the other hand, the disturbance travels quickly (about 20 m s^{-1}) through the central–eastern Pacific, significantly decreasing its amplitude. No longer is there evidence of a strict correlation between upper velocity potential and convective signals (dry–fast phase of the oscillation).

A second but weaker impulse is given to the disturbance over the convective areas of central and South America.

These results are in good agreement with the analyses of observed data by Knutson and Weickmann (1987) and von Storch and Xu (1990). This agreement is particularly noteworthy since we have used two independent sets of observational data: observed OLR from NOAA and 200-mb velocity potential from ECMWF analyses.

2) 200-MB EQUATORIAL ZONAL WIND

As described by the composites in Fig. 4, the oscillating signal detected by the POP analysis in the 200-mb velocity potential field propagates completely around the equator. However, as discussed in the introduction, χ is a useful large-scale parameter, but it does require cautious interpretation, and the propagation all around the equatorial belt should not be taken too literally (Slingo et al. 1995; Matthews 1994). The MJO was first detected in the wind field, and the perturbation of the upper-tropospheric zonal wind along the equator is generally considered an important feature of the oscillation. Therefore, in order to investigate if the propagating mode described by the dominant POP is also detectable in upper-zonal wind anomalies, composites of the equatorial (average 10°N–10°S) 200-mb zonal wind have been computed.

The composites are shown in Fig. 5 in the form of a Hovmöller diagram. They have been obtained from the band-pass filtered time series, and explain more than 10% of the filtered variance along most of the equator, with maxima of 25% over the Indian Ocean, and 15% over the Indonesian region, eastern Pacific, and equatorial America.

The composite patterns show a well-defined wavenumber one structure, with the largest values located over the Indian Ocean and eastern Pacific between the date line and equatorial America. The anomalies propagate eastward, and, from a visual inspection, the fea-

tures of their propagation appear to be consistent with the results previously found from tropical OLR and velocity potential. There is also a suggestion of a discontinuity in the propagation both in the Eastern and in the Western Hemispheres. The anomalies develop quickly over equatorial Africa and the Indian Ocean; they slow down between the Indonesian region and the central Pacific; they accelerate through the eastern Pacific as far as equatorial America, where they slow slightly before finally moving quickly through the Atlantic Ocean to equatorial Africa and the Indian Ocean.

The coherence between the oscillating modes detected in OLR, velocity potential, and zonal wind anomalies appears to be particularly good in the Eastern Hemisphere, where the signal in convection is strong. When the convective anomaly is located over the Indian Ocean (composite 1 and 2), significant westerly and easterly anomalies are found to the east and to the west of the enhanced convection region, respectively. Later, when the convective disturbance moves slowly through the west Pacific reaching its maximum amplitude (composite 3 and 4), the zonal wind perturbation increases, and maxima of easterly and westerly anomalies are found over the Indian Ocean and slightly to the east of the date line, respectively. These maxima, therefore, seem to be related to the strong and persistent convective activity sitting over the west Pacific.

3) DIVERGENCE

In a recent study, Hendon and Salby (1994) have investigated the evolution of the MJO in relation to anomalous convection. Using a regressive technique, they constructed composites of winds, divergence, temperature, and OLR. They found that the phase between anomalous convection and surface convergence evolves systematically during the life cycle of the disturbance: during amplification when inviscid convergence above the boundary layer (850 mb) remains phase locked with anomalous convection, surface convergence is positively correlated to anomalous convection so as to reinforce the anomaly, whereas during decay it is nearly in quadrature, providing little support to the convective anomaly.

Using the composite technique previously illustrated, we have computed the composites of the equatorial anomalous divergence at two reference locations, 85°E and 60°W, and at different pressure levels. The equatorial fields are defined by averaging between 5°N and 5°S, and besides the usual bandpass filter, all the fields have been spatially filtered retaining zonal wavenumbers 1–3, where most of the signal is concentrated. The longitudes of 85°E and 60°W have been chosen since these are equatorial locations where the velocity potential exhibits two relative maxima of variance, and since they appear to be fairly representative of the behavior of the oscillation in the respective hemispheres.

The plots of the vertical composites of the anomaly divergence at the two reference locations are shown in Fig. 6. Tropical divergence composite fields at the same pressure levels (not shown) show that the surface divergence has a predominant zonal wavenumber one structure and that all the anomaly fields have their largest activity in the Eastern Hemisphere. The 1000-mb divergence also exhibits a significant meridional structure: surface equatorial convergence is flanked by regions of divergence located at about 15° latitude north and south of the equator. This structure was also observed by Hayashi and Golder (1988) and Hendon and Salby (1994).

In Fig. 4, composite 1, enhanced convection (positive OLR anomaly) is located over the Indian Ocean, whereas reduced convection (negative OLR anomaly) is located between the Indonesian region and the date line. The enhanced convective anomaly coincides with convergence at the lower and divergence at the higher levels in composite 1 of Fig. 6a, and, in particular, there is a maximum of divergence at 200 mb. Therefore, the hypothetical cycle starts with a deep column of convergence from the surface up to 500 mb, and divergence at the top of the troposphere.

After about 5 days (composite 2), the convective anomaly (Fig. 4) and 200-mb divergence anomaly (Fig. 6a) at the reference location have both slightly decreased. At 700 mb the divergence has reached its minimum (maximum of convergence), whereas at lower levels, 850 and 1000 mb, the divergence has increased. At this stage of the oscillation the anomaly of enhanced convection sitting over the reference location lies above anomalous surface divergence, so the disturbance seems to be supported by the convergence at 700 and 500 mb.

In composite 3, the divergence at 1000 mb and 850 mb has increased. The maximum divergence anomaly at the surface is now reached, and at the same time, a cell of suppressed convection is developing (see Fig. 4), while the divergence at the top of the troposphere has become negative. The divergence at the intermediate levels, 500 mb and in particular 700 mb, is still negative, denoting a significant phase delay with respect to the levels below.

In composite 4, the divergence anomaly at 1000 mb is still strong, and it is out of phase with the anomaly at 200 mb. The latter is going to grow and reach its maximum in composite 5, in phase with the maximum of suppressed convection found in the OLR composites. Composite 5 is basically the opposite of composite 1, with strong convergence at the top of the troposphere and divergence at the lower levels. Divergence at 1000 mb and 850 mb, however, is in the decaying phase of its oscillation, in advance of the intermediate levels, 500 and 700 mb, where divergence is still in the growing phase.

In composite 6, about 25 days after starting the hypothetical cycle, the anomalous negative divergence has moved quickly from equatorial Africa to the Indian Ocean. The surface signal at the 85°E reference point

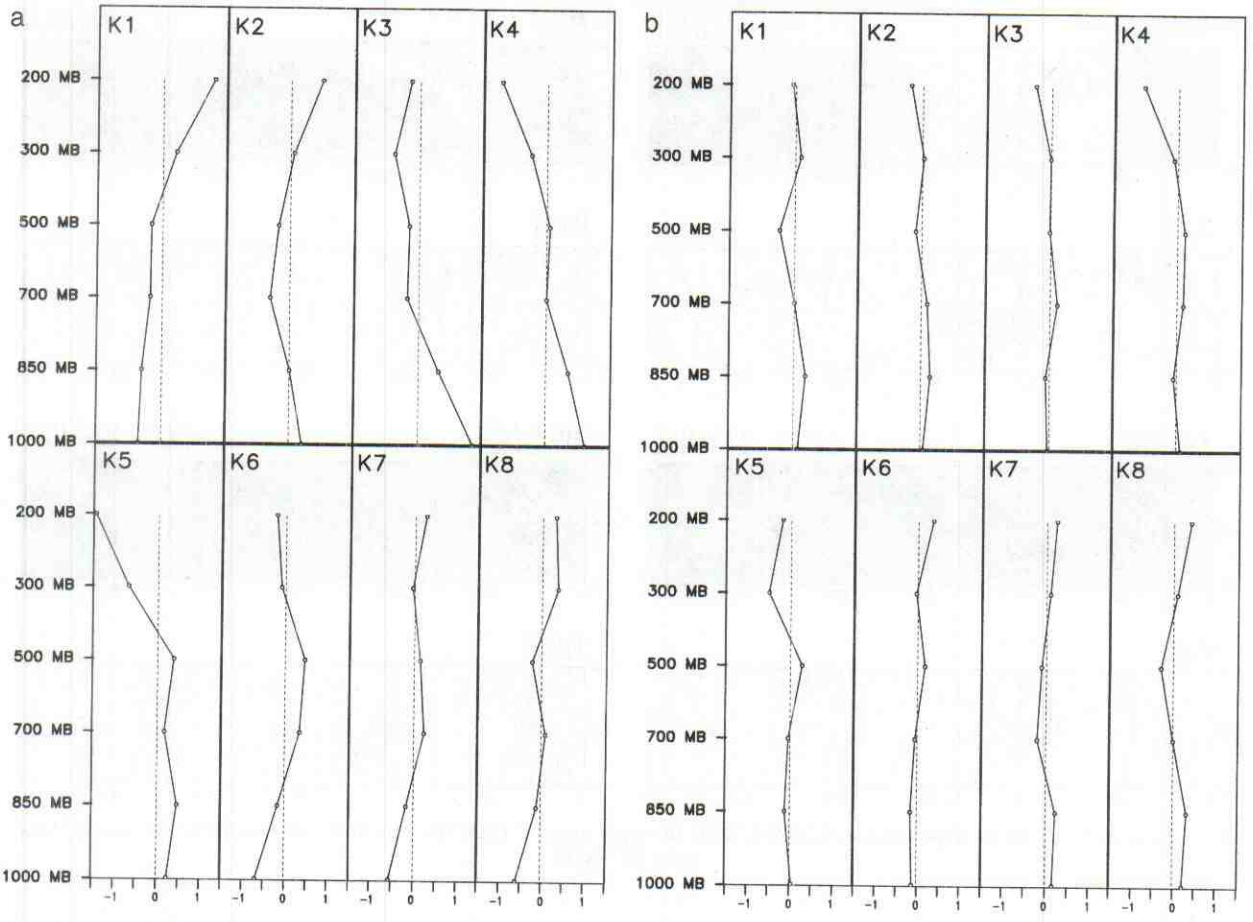

FIG. 6. Composites K_i of anomalous divergence (a) at 85°E and (b) at 60°W, and at different pressure levels, for ECMWF analyses. The values have been normalized by 1×10^{-6} s^{-1}.

reaches its minimum, in advance of the signal at 700 and 200 mb.

In the following two composites (7 and 8), the convergence anomoly at the surface keeps approximately its maximum value, while the convective signal develops and slowly moves from equatorial Africa to the Indian Ocean. The convection forced by the surface and 850-mb convergence takes about 15 days (three composite steps) to develop and reach maximum amplitude in composite 1.

The composites obtained from the time series of anomaly divergence over the reference point at 60°W are shown in Fig. 6b. Here, in agreement with the observation of a stronger signal in the Eastern than in the Western Hemisphere, there is evidence of a general and substantial reduction in the anomaly amplitude compared to the 85°E reference location (Fig. 6a).

At the top of the troposphere the divergence anomaly shows a significant amplitude (Fig. 6b), and it seems to be consistent with the oscillation depicted by the composites of χ and OLR, yet there is almost no signature in the low-level flow. In particular, at the surface the amplitude of the oscillation is very small, and it is hard to identify the existence of a clear and organized phase relationship between the oscillation at the different levels.

From composites similar to Fig. 6 computed over the western and the central Pacific (not shown), it was found that the reduction of the vertical phase shift occurs smoothly, moving from the Eastern to the Western Hemisphere.

The vertical structure of the oscillation has been studied by previous investigators (e.g., Murakami and Nakazawa 1985; Hayashi and Golder 1993) in observations and in model simulations. The vertical phase shift of equatorial anomalous divergence, in particular, seems to play an important role in the propagation of the disturbance, as theorized by Hendon and Salby (1994), because the leading convergence in the lower levels provides a moisture source for the midtropospheric convection. In the portion of the cycle over the Indian Ocean–western Pacific, the propagating midtropospheric convection grows easily on moisture-rich lower levels prepared by the leading convergence, presumably reinforcing convection.

The relationship between the vertical phase difference

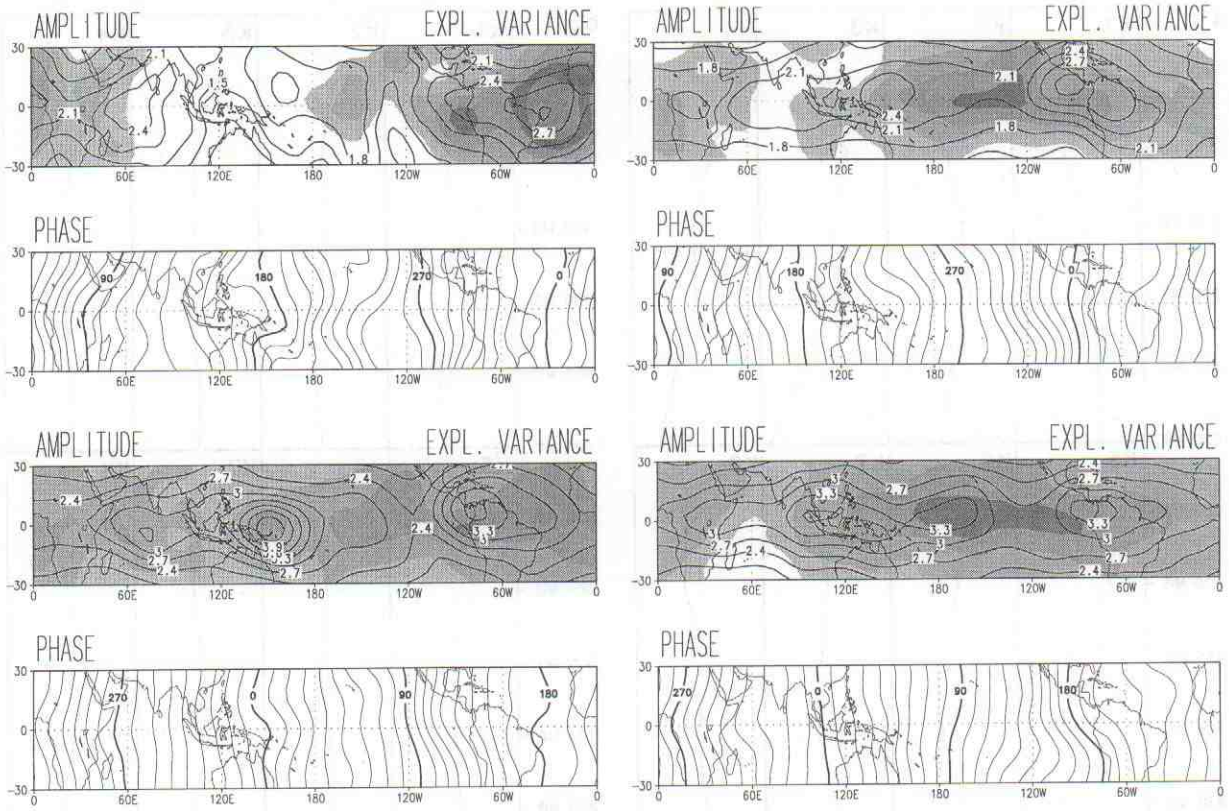

FIG. 7. Same as Fig. 3 but (a: upper left) for ECHAM3T106, (b: upper right) ECHAM3T42, (c: lower left) ECHAM3T21, and (d: lower right) ECHAM2.

and the velocity of propagation of the oscillation is not clear. However, it is noted that the vertical phase lag is generally larger and evolves coherently with the oscillation over the Indian Ocean, where the disturbance propagates slowly, whereas in the Western Hemisphere, where the oscillation has its faster propagation, there is no evidence of an organized phase relationship between anomalous divergence at the surface and at higher levels.

The main findings from the ECMWF analyses can be summarized as follows.

1) The POP analysis identifies an eastward traveling wavenumber one type pattern, which extends over the entire tropical region, with maximum variance over the Indian Ocean and the west Pacific. The signal, first identified in the χ anomaly field, is also detectable in anomalies of OLR, zonal wind, and divergence.
2) In agreement with von Storch and Xu (1990), the disturbance of χ travels with an eastward phase velocity of approximately 20 m s^{-1} over most of the global Tropics, but it slows down over areas with significant precipitation (Indian Ocean, west Pacific, and South America). Increasing propagation velocity is accompanied by decreasing wave amplitude, and vice versa.
3) The vertical structure of the oscillation in the Eastern Hemisphere gives evidence of the existence of an evolving phase shift between the surface and midlevels, especially 700 mb. In contrast, in the Western Hemisphere there is no evidence of an organized relationship between the phases of the oscillating signal at the different pressure levels.

4. Results: The MJO in the ECHAM models

In this section we show the results of the POP analysis performed on the output from the different GCM experiments.

For each experiment the equatorial POP modes are characterized by well-defined zonal wavenumber one patterns, high values of explained variance, and eastward propagation all around the equator with reasonably realistic periodicities (see Table 2).

The general features of the simulated modes and their properties of propagation will be described first by means of their associated tropical correlation patterns.

a. Associated correlation patterns

In Fig. 7, associated correlation patterns of the 200-mb tropical velocity potential for the different mod-

el versions are shown in the "amplitude phase" representation. As for the reference case (ECMWF analyses), we have chosen as zero phase the angle corresponding to the maximum amplitude. In all of the cases the oscillation is well defined over the entire tropical band, with largest amplitude centered across the equator and a fairly symmetrical decay away from the equator.

From the phase plot there is no evidence of a capability in the models to properly reproduce the change in phase speed between the Eastern and the Western Hemispheres, as observed in the reference case and already described in previous studies (e.g., von Storch and Xu 1990).

The mode simulated by the ECHAM3T106 model (Fig. 7a) seems to be slower in the Western than in the Eastern Hemisphere, and has its largest amplitude, of about 3×10^6 m^2 s^{-1}, around 30°W. The maximum of explained variance is located over this area and is rather large, more than 80%. Later on, the disturbance moves slowly over equatorial Africa, to the western Indian Ocean, where it amplifies and then accelerates, quickly crossing the Indian Ocean and the Indonesian region to the date line. Its amplitude decreases to its minimum value of about 1.5×10^6 m^2 s^{-1}, over the Maritime Continent. In the area between the Indian Ocean and the date line, the explained variance is small (less than 40%). Over the ITCZ and SPCZ, the phase plot shows the asymmetries already noticed in the ECMWF analyses, and here there is also some suggestion of a slowing down of the signal.

In the ECHAM3T42 case (Fig. 7b) the amplitude of the mode exhibits a more zonal pattern, and, also in this case, the simulated disturbance shows the strongest activity in the Western Hemisphere. The mode appears to travel slowly through the eastern Pacific, reaching a maximum amplitude (3×10^6 m^2 s^{-1}) off the Central American coast. In the Eastern Hemisphere the simulated mode shows two relative maxima of amplitude over the Indian Ocean and between the Indonesian region and the date line. On the other hand, over these areas the explained variance has its minimum, and, also in contrast with observations, the disturbance seems to move faster than in the Western Hemisphere.

The associated correlation patterns of the mode simulated by the ECHAM3T21 experiment are shown in Fig. 7c. The spatial distributions in the patterns exhibit characteristics closer to the observations than those obtained from the higher resolution versions of the model. The maximum of activity is confined to the Eastern Hemisphere, with the largest amplitude between the Indonesian region and the date line, and with a secondary maximum over the Indian Ocean. Even if the patterns are predominantly symmetric about the equator, the phase indicates some sensitivity to areas of convective activity, especially the ITCZ. The explained variance is generally high, especially over areas of large activity like the Indian Ocean, the Indonesian region, and equatorial America.

However, as in the other runs, there is no suggestion of a clear and consistent relationship between the amplitude of the mode and its velocity of propagation. The spatial distribution of the phase appears rather smooth along most of the equator, indicating that the propagation is characterized by an almost constant phase velocity. Only over the western part of South America and the Atlantic Ocean is there evidence of an acceleration.

The patterns representing the mode simulated by the ECHAM2 model (Fig. 7d) are markedly zonal with only a small modulation of the amplitude as a function of longitude. This leads the model to simulate disturbances characterized by poor sensitivity to the location of observed convection. The phase plot indicates that also in this experiment the mode tends to propagate with a rather constant phase velocity.

b. *Associated composite patterns*

1) 200-MB EQUATORIAL ZONAL WIND AND OLR

Figure 8 shows the composite patterns obtained from the band-pass filtered 200-mb equatorial zonal wind simulated by the models. The patterns obtained from the ECHAM3 simulations explain approximately 10% of the total filtered variance, with maxima larger than the 25% over the eastern Pacific, whereas in the ECHAM2 case the explained variance is only about 5%–6% along most of the equatorial belt.

The oscillation detected in the simulated upper-tropospheric zonal wind appears to be consistent with the results shown by the χ patterns. In all the experiments there is evidence of a wavenumber one disturbance that propagates eastward completely around the equator. As for the χ fields, the zonal wind anomalies seem to propagate with a practically constant phase velocity, without showing the discontinuities observed in the reference case.

In the ECHAM3 experiments the amplitude of the anomalies is comparable to that observed in the ECMWF analyses, but the longitudinal distribution of their maxima appears to be substantially different from the reference case. In particular, the maxima over the Indian Ocean appear westward shifted compared to the analyses, especially in the higher-resolution versions of the model. There is also a clear suggestion of an amplification of the oscillation over the eastern Pacific, which has previously been observed in the zonal wind perturbation associated with the MJO simulated by a number of GCMs (e.g., Slingo et al. 1995).

In the ECHAM2 case, the perturbation of the zonal wind associated with the simulated oscillation appears substantially weaker and rather uniform along the equator. The weakness of the disturbance, and its lack of longitudinal modulation, might be due to the less realistic convective driven tropical circulation that the Kuo scheme seems to give compared to the Tiedtke convective parameterization (Tiedtke 1989). In partic-

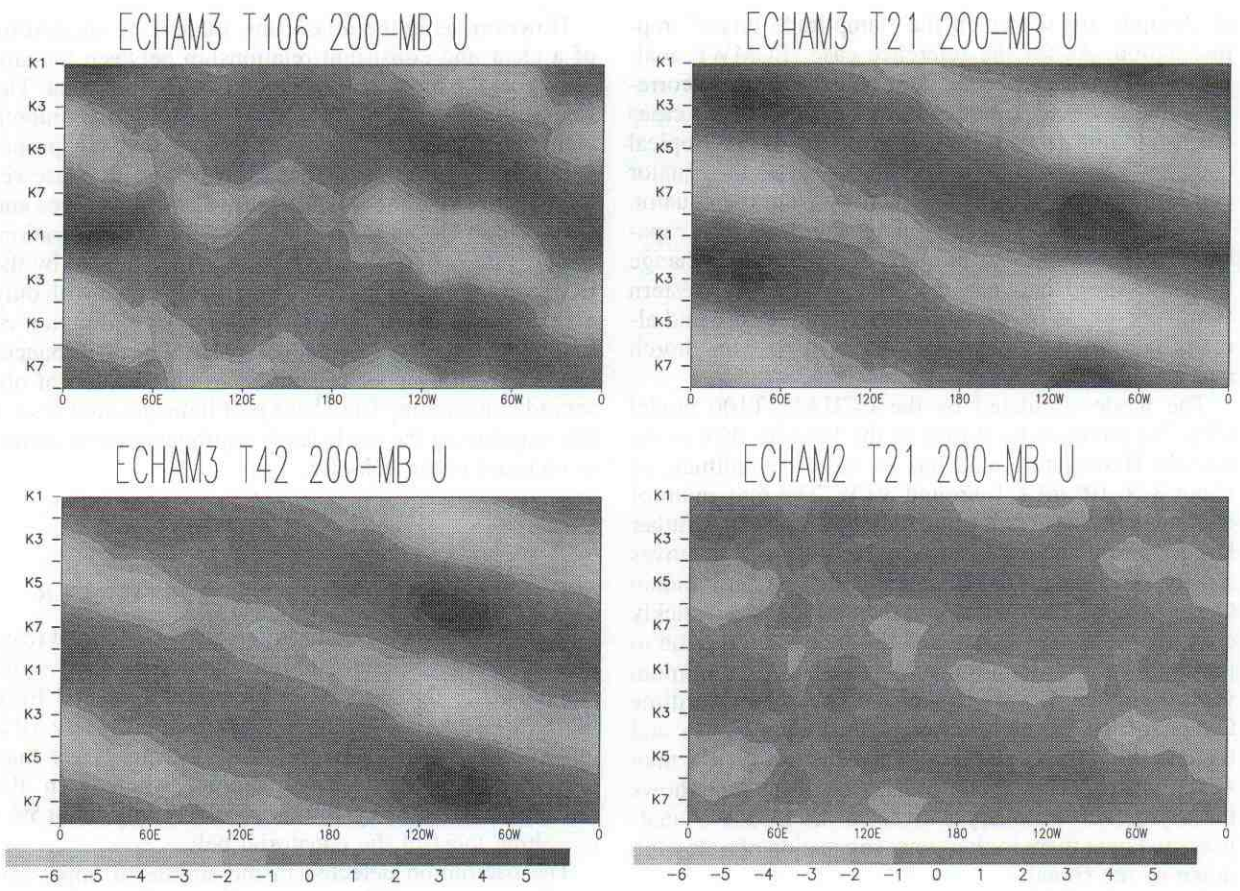

FIG. 8. (a: left) Same as Fig. 5 but for the ECHAM3T106 (top panel) and ECHAM3T42 (bottom panel) models. (b: right) Same as (a) but for the ECHAM3T21 (top panel) and ECHAM2 (bottom panel) models.

ular, it might be related to the Kuo scheme's failure to generate strong intraseasonal variations in forcing from convective heating over the west Pacific–Indian Ocean regions.

An assessment of the simulated intraseasonal oscillation of convection, associated with the dominant POP mode, is given in terms of composites of anomalous OLR (Fig. 9). The composites are computed from band-pass-filtered time series of OLR anomaly produced by ECHAM2 and ECHAM3 and explain, on average, about 8% and 6% of the total filtered variance for ECHAM3 and ECHAM2, respectively.

In the ECHAM3 model the composites exhibit at all resolutions (Figs. 9a,b, top panel) maxima over the Indian Ocean, the west Pacific, and equatorial America. From a visual inspections these disturbances seem, in general, consistently correlated with the oscillation of the zonal wind anomalies. The ECHAM2 model, on the other hand, exhibits a generally weak perturbation of OLR, and, as also observed for the upper-tropospheric zonal wind, a small longitudinal modulation of the amplitude (Fig. 9b, bottom panel). Therefore, as also noted by Slingo et al. (1995), a poor dynamical response in terms of the zonal wind field, as in ECHAM2, might be related to a poor modulation of forcing from convective heating at intraseasonal time scales.

2) DIVERGENCE

Among the different versions of the ECHAM model, the T21 version of ECHAM3 is the one that produces the strongest intraseasonal oscillation in the Eastern Hemisphere. In this experiment there is also some suggestion of a consistent correlation between the amplitude of the oscillation and the observed longitudinal distribution of convective activity. These results are also confirmed by composites of anomaly divergence obtained from the different experiments (not shown), and hence, in the following, we limit our discussion of the vertical composites of equatorial divergence to the T21 version of the ECHAM3 model.

The composites of the spatially and time-filtered anomalous divergence have been computed at six pressure levels, following the same procedure as used for the ECMWF analyses.

An inspection of the maps of the tropical divergence composite fields (not shown) reveals that the patterns obtained from the model have a more pronounced zonal

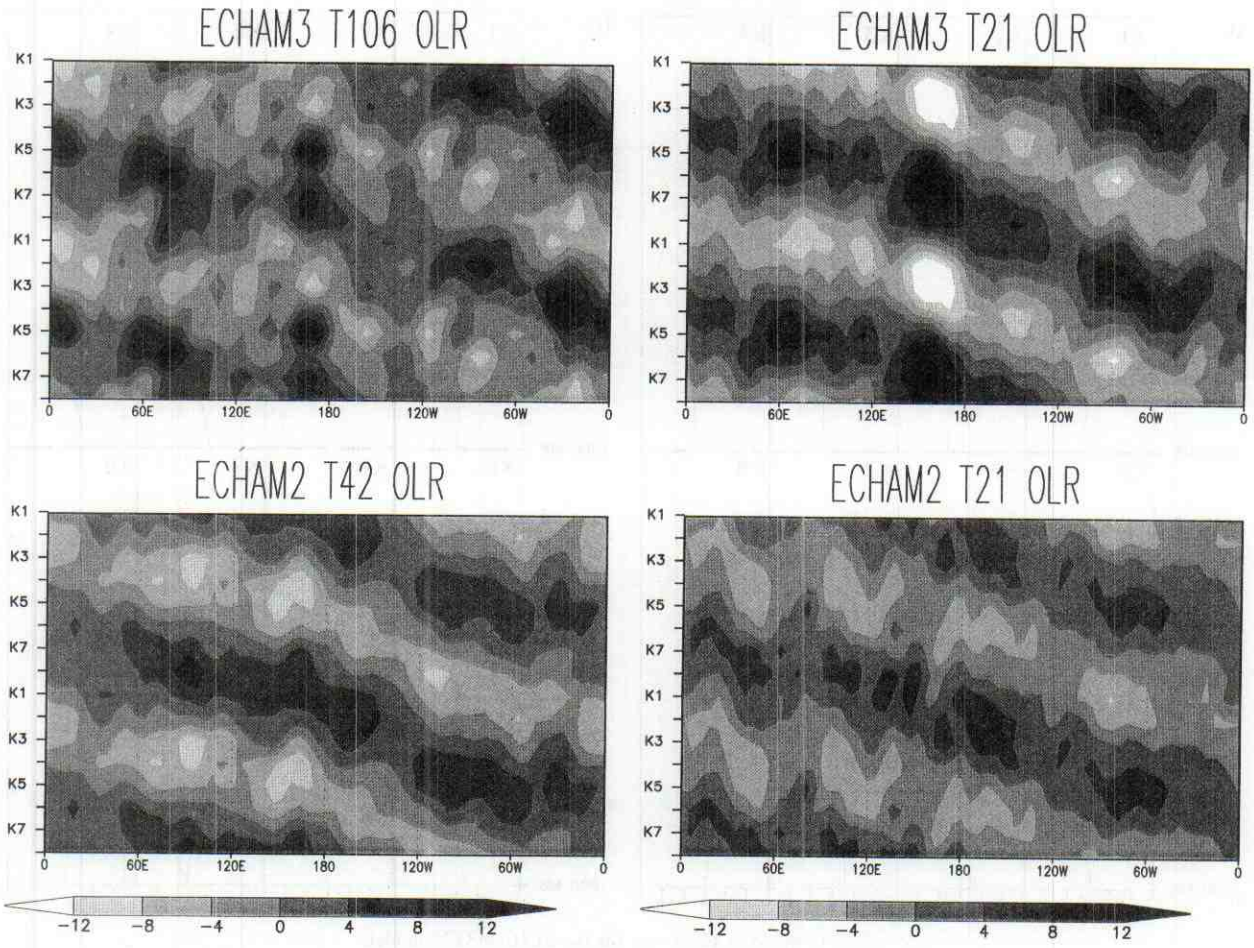

FIG. 9. Same as Fig. 8 but for equatorial OLR anomaly. Shaded contour interval is 4 W m^{-2}.

wavenumber one structure and a less significant meridional component than the patterns obtained from the ECMWF analyses.

The vertical profile of the composite patterns at the reference locations of 85°E and 60°W along the equator are shown in Figs. 10a and 10b, respectively. The large activity found in the χ field in the Western Hemisphere, and in particular over equatorial America, is confirmed by the vertical composites at 60°W, where the amplitude of the oscillation is comparable to the amplitude at 85°E. In the Eastern Hemisphere, the amplitude of the simulated signal appears to be substantially less than observed, especially at 1000 mb.

In Fig. 10a, composite 1, the large divergence anomaly at the top of the troposphere lies over divergence at the surface and convergence at the intermediate levels. In the next three composites (composites 2, 3, and 4), the divergence at the surface practically maintains its maximum value, whereas the signal at the higher levels, in particular at 700 mb, exhibits a significant delay, reaching the maximum of divergence only between composites 4 and 5. The anomalies at 700 and 500 mb, which oscillate in phase, are nearly perfectly opposite in phase to the signal at the top of the troposphere.

Composites 5, 6, 7, and 8 are characterized by convergence at the surface. In the meantime, the signal at 700 mb passes from its maximum of divergence (composite 5), to its maximum of convergence (composite 8 and composite 1). The oscillation at this level, therefore, appears to lag about 10–15 days with respect to the surface, whereas it seems to evolve in phase with the oscillation at 500 mb and in opposite phase with 300 and 200 mb.

In the first half of the life cycle of the oscillation, the surface divergence leads the vertical signal, reaching its maximum values very quickly, and then keeping this value and waiting for the higher levels. About 15 days after starting the cycle (composite 4), the surface anomaly has been caught up by the midlevels, in particular 700 mb, giving rise to a deep cell of divergence from 1000 mb up to 500 mb, opposite in phase to convergence at the top of the troposphere. In the second half of the cycle the oscillation starts with surface convergence. The signal then develops in the midlevels to give a deep

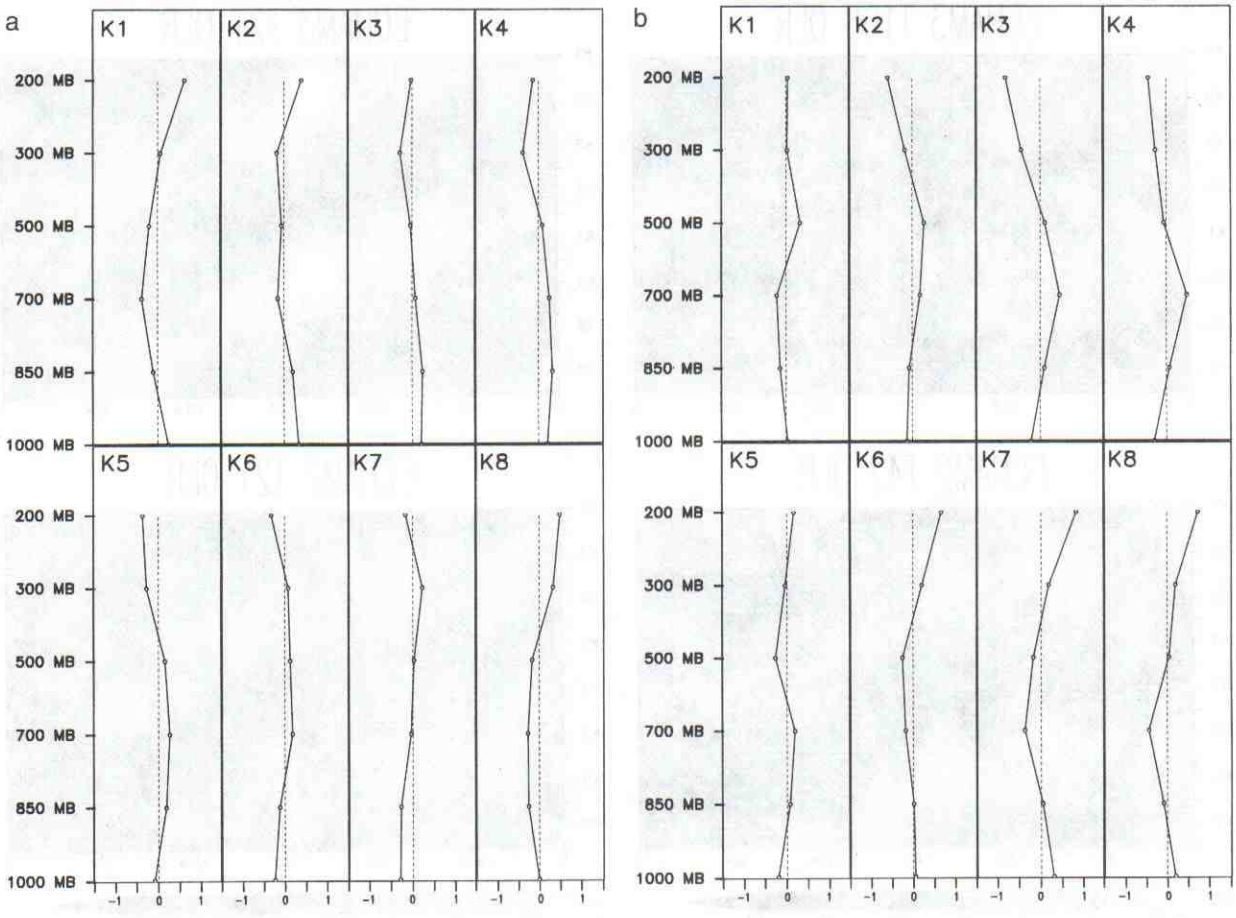

FIG. 10. Same as Fig. 6 but for the ECHAM3T21 model.

cell of convergence, opposite in phase to the divergence at the highest levels.

The composites computed from the anomaly at 60°W are shown in Figure 10b. As already noticed, the amplitude of the oscillation achieves large values, especially at 700 and 200 mb. Also its vertical phase evolution is substantially different from the results obtained in the Eastern Hemisphere: the anomalies at 1000 and 200 mb seem to oscillate nearly in phase and both of them in opposition with the signal at 700 mb.

5. Summary and conclusions

The intraseasonal variability of the tropical atmosphere simulated by different versions of the ECHAM GCM has been analyzed and compared with ECMWF analyses. To demonstrate the effect of improved model physics and improved horizontal resolution on the simulated oscillation, we have used climatological GCM experiments carried out with the second (ECHAM2) and the third (ECHAM3) generation of the ECHAM GCM, and with three horizontal resolution versions of the ECHAM3 model (triangular truncation 21, 42, and 106, referred to as T21, T42, and T106, respectively).

A qualitative inspection of the Hovmöller diagrams of the band-pass filtered 200-mb equatorial velocity potential has revealed that an eastward propagating disturbance, characterized by a zonal wavenumber one structure and a period of several weeks, is present both in the ECMWF analyses and in the output of all the ECHAM models that were studied.

Following the diagnostic approach pursued by von Storch and Xu (1990), the characteristics of these disturbances have been investigated by means of a POP analysis. The POP analysis was performed on the 200-mb equatorial velocity potential. Once the dominant POPs were defined for the equatorial field, the POP coefficients were used to derive associated composite and correlation patterns for tropical 200-mb velocity potential, OLR, upper-tropospheric zonal wind, and divergence.

In all of the analyzed cases, one dominant POP pair, with zonal wavenumber one spatial structure, was found. The disturbances travel eastward with periods between 36 days (ECHAM3T106 case) and 42 days (ECMWF analyses). The associated correlation and composite patterns show that in the ECMWF analyses as well as in each experiment, the signal is not limited

to the equator, but extends over the entire tropical region. The oscillation patterns are also fairly symmetrical with respect to the equator, except for the extremes located over the Pacific ITCZ and the southern tip of India, which are shifted slightly northward.

In the ECMWF analyses the traveling mode has its largest amplitude and slowest propagation in the Eastern Hemisphere. As the amplitude phase diagram and the composite patterns have pointed out, there are two peaks of activity: one over the Indian Ocean and one between the Indonesian region and the date line. The results obtained from the ECMWF analyses confirm the results of von Storch and Xu (1990), who used an independent dataset (NMC analyses).

The characteristics of the anomalous divergence signal caught by the dominant POP mode in the ECMWF dataset at different pressure levels and depicted by the composites shown in Fig. 6 resemble the results found by Hendon and Salby (1994) with their regressive technique. During the course of the disturbance life cycle, the surface divergence anomaly seems to lead the signal at the midlevels. There is also evidence that the phase lag between anomalous convection and convergence at 700 and 1000 mb changes when the disturbance moves from the Eastern to the Western Hemisphere.

From the two-dimensional composites (not shown), it turns out that the surface divergence anomaly appears to propagate across the Eastern Hemisphere slightly faster than the anomalies of the upper-tropospheric divergence and OLR. This difference in the phase velocities is probably responsible for the phase alteration.

A noteworthy difference from the Hendon and Salby results is the raising of the level at which the significant phase lag is found in our results. It is conceivable that the different level at which the phase shift occurs in our results might be related to some change in the parameterization schemes of the ECMWF analysis system, which could have produced a slightly deeper boundary layer. In 1989 important changes in the analysis scheme were made, including replacement of the radiation scheme and replacement of the Kuo convection by a mass-flux scheme (Arpe 1990).

Even if the ECHAM3 physics differs from that in ECHAM2 in many respects, the most important difference seems to be the change from the Kuo scheme to the Tiedtke convection scheme. The resulting improvement in the simulated tropical intraseasonal variability is significant. In the ECHAM2 case, the simulated oscillation exhibits a weak response both in the upper-tropospheric zonal wind and OLR anomalies. At intraseasonal timescales, the perturbation of these fields, associated with the dominant POP mode, appears to be weakly active all around the equator, without showing any significant modulation of the amplitude with longitude. In the ECHAM3T21 case, on the other hand, the signal detected in velocity potential, zonal wind, and OLR anomalies seems to be coherently modulated by the convective regions of the Eastern Hemisphere and equatorial America. Therefore, at low resolution the ECHAM3 model seems to give a more favorable comparison with the observations, at least in terms of spatial distribution of the simulated oscillation.

Moreover, the vertical composites of the anomaly divergence, computed for the ECHAM3T21 model, show a significant phase lag between 1000-mb and 700-mb levels, and, in the Eastern Hemisphere, this phase lag appears to evolve coherently with the cycle of the oscillation as observed in the reference case.

The increased resolution leads to less favorable results. In fact, the disturbances simulated by the high-resolution versions of the ECHAM3 model, T42 and T106, in evident contrast with the ECMWF analyses, have smaller amplitude in the Eastern than in the Western Hemisphere. In particular the west Pacific and Indonesian regions seem to be only marginally affected by the oscillation, whereas there is an overproduction of activity over central and equatorial America.

Finally, although in all experiments the simulated oscillation appears to propagate eastward around the equatorial belt with reasonable periodicity, none of the models have correctly reproduced the discontinuities in phase speed that seem to characterize the propagation of the observed disturbance. The generally poor agreement between the observed and the simulated features of propagation suggests that at least some of the processes responsible for the MJO, and most plausibly those involving the convective scheme, are still elusive in this formulation of the model.

Acknowledgments. The authors are endebted to Dr. Neil Ward for helpful comments and support with the language and to Prof. Lennart Bengtsson for providing the T106 simulated data. They also thank the staff of the Max-Planck-Institut für Meteorologie in Hamburg, where most of this work was performed.

This research has been supported by the European Community bursary in the Environment Program (Climatology and Natural Hazards) Contract ERB-EV5V-CT-93-5212. One of the authors (A. Navarra) wishes to acknowledge the support of the EU contract Medium Term Climate Variability Project (EV5V-CT92-0121).

REFERENCES

Arkin, P. A., and P. E. Ardanuy, 1989: Estimating climatic-scale precipitation from space: A review. *J. Climate,* **2,** 1229–1238.

Arpe, K., 1990: Impacts of changes in the ECMWF analysis-forecasting scheme on the systematic error of the model. *ECMWF Seminar on 10 Years of Medium-Range Weather Forecasting,* Reading, England, ECMWF, 69–114.

Born, M., and E. Wolf, 1975: *Principles of Optics.* Pergamon Press, 808 pp.

Chang, C. P., and H. Lim, 1988: Kelvin wave-CISK: A possible mechanism for the 30–50 day oscillations. *J. Atmos. Sci.,* **45,** 1709–1720.

Emanuel, K. A., 1987: An air–sea interaction model of intraseasonal oscillation in the tropics. *J. Atmos. Sci.,* **44,** 2324–2340.

Ferranti, L., T. N. Palmer, F. Molteni, and E. Klinker, 1990: Tropical–

extratropical interaction associated with the 30–60 day oscillation and its impact on medium and extended range prediction. *J. Atmos. Sci.*, **47,** 2177–2199.

Hasselmann, K., 1988: PIPs and POPs: The reduction of complex dynamical systems using principal interaction and oscillation patterns. *J. Geophys. Res.*, **93,** 11 015–11 021.

Hayashi, Y., and D. G. Golder, 1988: Tropical intraseasonal oscillation appearing in a GFDL general circulation model and FGGE data. Part II: Structure. *J. Atmos. Sci.*, **45,** 3017–3033.

——, and ——, 1993: Tropical 40–50 and 25–30-day oscillations appearing in realistic and idealized GFDL climate models and the ECMWF dataset. *J. Atmos. Sci.*, **50,** 464–494.

Hendon, H. H., and M. L. Salby, 1994: The life cycle of the Madden–Julian oscillation. *J. Atmos. Sci.*, **51,** 2225–2237.

Ju, J.-H., and J. Slingo, 1995: The Asian summer monsoon and ENSO. *Quart. J. Roy. Meteor. Soc.*, **121,** 1133–1168.

Knutson, T. R., and K. M. Weickmann, 1987: 30–60 day atmospheric oscillations: Composite life cycles of convection and circulation anomalies. *Mon. Wea. Rev.*, **115,** 1407–1436.

Kuma, K., 1990: Diabatic heating and the low frequency dynamics in the tropics. *Meteor. Atmos. Phys.*, **44,** 265–279.

——, 1994: The Madden and Julian oscillation and the tropical disturbances in an aqua-planet version of JMA global model with T63 and T159 resolution. *J. Meteor. Soc. Japan,* **72,** 147–172.

Kuo, H. L., 1974: Further studies of the parameterization of the influence of cumulus convection on large-scale flow. *J. Atmos. Sci.*, **31,** 1232–1240.

Lau, K. M., and P. H. Chan, 1985: Aspects of the 40–50 day oscillation during the northern winter as inferred from outgoing longwave radiation. *Mon. Wea. Rev.*, **113,** 1889–1909.

——, and ——, 1986: The 40–50 day oscillation and the El Nino/Southern Oscillation—A new perspective. *Bull. Amer. Meteor. Soc.*, **67,** 533–534.

——, and L. Peng, 1987: Origin of low-frequency (intraseasonal) oscillations in the tropical atmosphere. *J. Atmos. Sci.*, **44,** 950–972.

——, and P. H. Chan, 1988: Interannual and intraseasonal variations of tropical convection: A possible link between the 40–50-day oscillation and ENSO? *J. Atmos. Sci.*, **44,** 506–521.

Lorenc, A. C., 1984: The evolution of planetary-scale 200 mb divergent flow during the FGGE year. *Quart. J. Roy. Meteor. Soc.*, **110,** 427–441.

Madden, R. A., 1986: Seasonal variation of the 40–50 day oscillation in the tropics. *J. Atmos. Sci.*, **43,** 3138–3158.

——, and P. R. Julian, 1971: Detection of a 40–50 day oscillation in the zonal wind in the tropics. *J. Atmos. Sci.*, **28,** 702–708.

——, and ——, 1972: Description of global-scale circulation cells in the tropics with a 40–50 day period. *J. Atmos. Sci.*, **29,** 1109–1123.

——, and ——, 1994: Observations of the 40–50-day tropical oscillation—A review. *Mon. Wea. Rev.*, **122,** 814–837.

Matthews, A. J., 1994: The intraseasonal oscillation. Ph.D. dissertation, University of Reading, 220 pp.

Murakami, T., and T. Nakazawa, 1985: Tropical 45 day oscillation during the 1979 Northern Hemisphere summer. *J. Atmos. Sci.*, **42,** 1107–1122.

Neelin, J. D., I. M. Held, and K. H. Cook, 1987: Evaporation–wind feedback and low-frequency variability in the tropical atmosphere. *J. Atmos. Sci.*, **44,** 2341–2348.

Park, C.-K., D. M. Straus, and K.-M. Lau, 1990: An evaluation of the structure of tropical intraseasonal oscillation in three general circulation models. *J. Meteor. Soc. Japan,* **68,** 403–417.

Roeckner, E., and Coauthors, 1992: Simulation of the present-day climate with the ECHAM model: Impact of model physics and resolution. Max-Planck-Institut für Meteorologie Rep. 93, 172 pp. [Available from Max-Plank-Institut für Meteorologie, Bundesstrasse 55, D-20146 Hamburg, Germany.]

Rui, H., and B. Wang, 1990: Development characteristics and dynamic structure of tropical intraseasonal convection anomalies. *J. Atmos. Sci.*, **47,** 357–379.

Salby, M. L., and H. H. Hendon, 1994: Intraseasonal behavior of clouds, winds, and temperature in the Tropics. *J. Atmos. Sci.*, **51,** 2207–2224.

Slingo, J. M., and Coauthors, 1995: Intraseasonal oscillation in 15 atmospheric general circulation models (results from an AMIP diagnostic subproject). World Meteorological Organization WCRP-27, 32 pp. [Available from World Meteor. Org., Case Postale No. 2300, CH-1211, Geneva 20, Switzerland.]

Tiedtke, M., 1989: A comprehensive mass flux scheme for cumulus parametrization in large-scale models. *Mon. Wea. Rev.*, **117,** 1779–1800.

Trenberth, K. E., 1992: Global analyses from ECMWF and atlas of 1000 to 10 mb circulation statistics. NCAR Tech. Note NCAR/TN-373+STR, 191 pp. [Available from NCAR Information Services, P.O. Box 300, Boulder, CO 80307.]

von Storch, H., and J. Xu, 1990: Principal Oscillation Pattern analysis of the tropical 30- to 60-day oscillation. Part 1: Definition of an index and its prediction. *Climate Dyn.*, **4,** 175–190.

——, T. Bruns, I. Fischer-Bruns, and K. Hasselmann, 1988: Principal Oscillation Pattern analysis of the 30- to 60-day oscillation in a general circulation model troposphere. *J. Geophys. Res.*, **93,** 11 022–11 036.

——, G. Buerger, R. Schnur, and J. S. von Storch, 1995: Principal Oscillation Patterns: A review. *J. Climate,* **8,** 377–400.

Wang, B., 1988: Dynamics of tropical low-frequency waves: An analysis of the moist Kelvin wave. *J. Atmos. Sci.*, **45,** 2051–2065.

Weickmann, K. M., and S. J. S. Khalsa, 1990: The shift of convection from the Indian Ocean to the western Pacific Ocean during a 30–60-day oscillation. *Mon. Wea. Rev.*, **118,** 964–978.

——, G. R. Lusky, and J. E. Kutzbach, 1985: Intraseasonal (30–60) fluctuations of outgoing longwave radiation and 250-mb streamfunction during northern winter. *Mon. Wea. Rev.*, **113,** 941–960.

Yamagata, T., and Y. Hayashi, 1984: A simple diagnostic model for the 30–50 day oscillation in the tropics. *J. Meteor. Soc. Japan,* **62,** 709–717.